Biocompatible Neodymium-Doped Nanocrystals as Probes for Diffraction-limited, *in vitro* Temperature Sensing

Bravo, M.[ab], Yang, S.[a], Brooke, S.[a], Wen, D.[a], Taemaitree, F.[c], Zaman, S.[ab], Uji-i, H.[b,c], Rocha, S.[b], Mulvaney, P.[a], Hutchison, J.[a*]

[a] ARC Centre of Excellence in Exciton Science, School of Chemistry University of Melbourne Parkville, VIC 3010, Australia;
[b] Molecular Imaging and Photonics, Chemistry Department, KU Leuven, Celestijnenlaan 200F, 3001 Heverlee, Belgium;
[c] Research Institute for Electronic Science (Ries), Hokkaido University, N20W10, Kita ward, Sapporo, 001-0020 Hokkaido, Japan;
***** Correspondence: james.hutchison@unimelb.edu.au

Abstract: Localized hyperthermia is a promising approach to cancer therapy. However, its clinical potential is limited by heterogeneous heat distribution within tumors, and improved methods to measure temperature at the sub-micron level are required. To address this challenge, luminescent nanothermometers, such as lanthanide-doped nanocrystals (Ln-NC) operating in the near-infrared (NIR), have been investigated for accurate spatiotemporal thermal monitoring. In this study, the synthesis of neodymium-doped, sodium yttrium fluoride nanocrystals ($NaYF_4$) was optimized to achieve high photoluminescence (PL) under NIR irradiation by adjusting the dopant concentration and by shelling with inert layers. Standard curves for luminescence-based temperature readout were developed using ratiometric analysis of the temperature-dependent PL spectra in the 850-920 nm biological window. A silica shell was added to the particles and shown to confer excellent aqueous stability and cellular uptake in A549 lung cancer cells, with cell viability maintained >85% when incubated with up to 50 µg/ml of the silica-shelled particles over 6 hours. Finally, luminescent thermal readout was demonstrated *in vitro* in A549 cells by spectrally resolving the diffraction-limited luminescence spots from single particles over a clinically relevant temperature range from 20-50 °C. The demonstration of biocompatible, nanoscale, NIR thermometry in cells is a significant step in the development of viable hyperthermal cancer treatments.

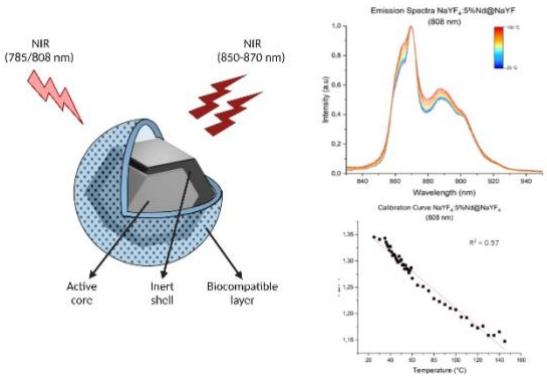

Key Words: Luminescence nanothermometers; Single NP thermometry; Cancer hyperthermia;

1. Introduction

Subjecting tumors to localized hyperthermia is an important cancer therapy, and targeting tumors with heat-generating nanoparticles (nanoparticle hyperthermia, NP-HT) is one of the most exciting new directions[1,2]. NPs within the size range of 20 and 200 nm can extravasate leaky tumor blood vessels and accumulate at the tumor site via the enhanced permeability and retention (EPR) effect. Surface-functionalization of NPs with moieties that specifically bind to tumor biomarkers further aids active tumor targeting[6,7]. This tumor-specific NP accumulation allows for higher therapeutic specificity and leads to a lower probability of off-target toxicity to healthy tissues, making NP-HT an exciting alternative to currently available therapies[8]. HT exploits artificial rises in temperature above optimal physiological values over a certain time to induce a heat shock reaction in cells[9]. For temperatures between 40-45 °C (low and moderate hyperthermia), blood profusion and vascular permeability at the tumor site are increased, simultaneously enhancing drug delivery efficiency and tumor oxygenation. As a result, HT can enhance sensitivity to chemo and radiotherapy, potentially enhancing the outcomes of difficult-to-cure cancers[10,11]. Temperatures above 45 °C can lead to irreversible cell damage, directly destroying cancerous cells through thermal ablation[8,9,12]. While HT provides a promising alternative as a standalone therapy or as an adjuvant for other anti-tumor approaches, several challenges remain in translating promising results to the clinic. One of the main hurdles is the heterogeneous heat distribution within the tumor, as well as off-target temperature increases and subsequent damage to surrounding healthy tissue. To address this limitation, accurate spatiotemporal and thermal profiling in solid tumors during HT is essential for the design of effective therapeutic outcomes with minimal side-effects, by enabling the fine-tuning of therapeutic parameters[8,13].

Most HT procedures to date employ contact thermometers, such as thermocouples and fiber optic sensors, which offer high thermal resolution but are invasive and limited to single-point thermal readouts within a tumor[14–16]. Infrared (IR) imaging is a non-contact alternative with high thermal and spatial resolution[16], but is restricted to superficial temperature sensing due to tissue emissivity[17,18]. Once again nanoparticles may provide the solution, enabling non-contact, real-time temperature readouts even from sub-cutaneous tumors during HT[19,20]. Luminescent nanothermometers display relevant

temperature-dependent emission in the physiological and above-physiological temperature range, which can be used to derive local temperature with sub-micron spatial resolution[16]. Over the past couple of decades, different temperature-sensitive nanoprobes have been developed. In particular, lanthanide-doped nanocrystals (Ln-NCs) have emerged as ideal candidates, since they exhibit low phototoxicity and do not photobleach. Ln-NCs comprise a optically transparent crystal host, that is doped with varying concentrations of one or more lanthanide ions (Ln^{3+}) [21]. Neodymium (Nd^{3+}) is one of the most widely studied Ln^{3+} for bio-sensing and bio-imaging applications, mainly because it exhibits excitation and emission lines within the first biological transparency window in the NIR (800-950 nm)[16]. In this spectral region, light absorption and scattering by biological tissue is reduced, improving the penetration of optical excitation and luminescent temperature readout. [16,19].

In this work we explore the design of biocompatible Nd^{3+}-doped NCs (Nd-NCs) for precise temperature monitoring inside biological environments. Sodium yttrium fluoride ($NaYF_4$) was chosen as the host material, due to its high optical transparency, and its low phonon energies which minimize nonradiative multiphonon relaxation processes that quench dopant luminescence[22,23]. Additionally, $NaYF_4$ offers a robust matrix which can accommodate the lanthanide ions without significantly disrupting the lattice structure [24].

Here we synthesize Nd-NCs via a thermal decomposition method and optimize their photoluminescence (PL) by tuning the dopant concentration and adding a protective inert $NaYF_4$ shell (Nd-NC@shell). To reduce cytotoxicity and ensure aqueous stability, the as-synthesized Nd-NC@shell particles were encapsulated inside a biocompatible silica (SiO_2) layer (Nd-NC@shell@SiO_2). We use NIR excitation (785 nm and 808 nm lasers) to generate temperature-dependent, multi-peaked Nd emission between 850-920 nm, from which we can construct standard curves of temperature vs luminescence peak ratio. We show that the Nd-NC@shell@SiO_2 particles are efficiently incorporated into A549 cancer cells without compromising cell viability. Most importantly, we use luminescence imaging and microspectroscopy at low particle loadings to resolve the diffraction-limited emission point spread functions from single particles within A549 cells. Single particle spectra are found to vary with temperature over the range 20-50 °C *in vitro*, demonstrating the applicability of our NPs as local temperature probes in biological environments. This work provides crucial information on the use of Ln-doped nanothermometers in preclinical HT studies, and helps guide the rational design of next-generation nanomaterials for targeted light-mediated cancer therapies.

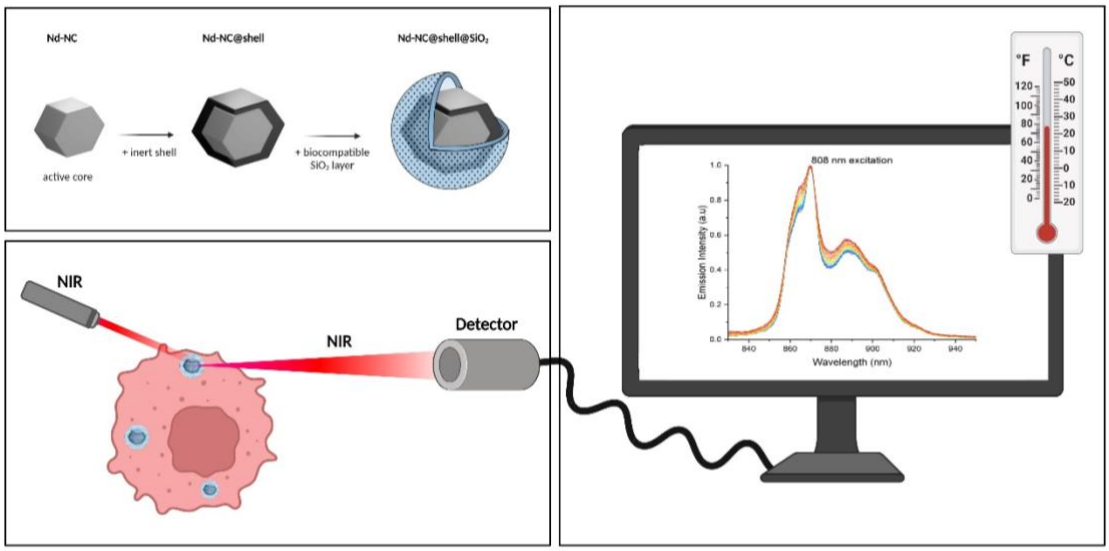

Figure 1| Schematic representation of the synthesis and modification of the synthesized neodymium-doped nanocrystals (Nd-NCs). Active cores consisting of Nd^{3+} doped $NaYF_4$ lattices were synthesized via thermal decomposition. The active cores were then modified with an inert $NaYF_4$ shell, generating Nd-NC@shell NPs. Lastly, a silica layer was added for stability in aqueous medium and reduced cytotoxicity, leading to the formation of Nd-NC@shell@SiO_2 NPs. Biocompatible Nd-NC@shell@SiO_2 were used as nanothermometers, displaying temperature-dependent spectral shape.

2. Materials and Methods

2.1. Materials

Sodium trifluoroacetate ($Na(CF_3COO)_3$, 98%), trifluoroacetic acid (TFA, 99%), Yttrium(III) oxide (nanopowder, <50 nm particle size), 1-Octadecene- (ODE, 90%), oleic acid (OA, 90%), Tetraethyl Orthosilicate (TEOS, 98%), IGEPAL® CA-

630, Ammonium hydroxide (NH_4OH, 28-30%), Cyclohexane (≥ 99.8%), and Poly(methyl methacrylate) (PMMA), were purchased from Sigma-Aldrich; Neodymium oxide was purchased from Koch-Light Laboratories Ltd; Polyethylene Glycol (PEG, MW 8000) was purchased from MP Biomedicals; Dulbecco's modified eagle medium (DMEM), Gentamicin, Dulbecco's phosphate Buffered saline (PBS, no calcium, no magnesium), Formaldehyde (4% in PBS), trypsin-EDTA (0.5%), and Hank's balanced salt solution (HBSS, no phenol red) were purchased from Wako Pure Chemical Industries; Triton X-100 (0.1%) was purchased from Nacalai Tesque, INC; Alexa Fluor 488 Palloidin 488 , Vybrant® DiO cell-labeling solution, and L-glutamine were purchased from Thermofisher Scientific; Fetal bovine serum (FBS) was purchased from Gibco; Cell Counting Kit-8 (CCK-8) was purchased from Dojindo; Milli-Q water is from Millipore. All the chemicals were used without further purification.

2.2. Methods

Preparation of Lanthanide Fluoroacetate Precursors: Lanthanide fluoroacetate precursors were prepared by mixing 500 mg of Nd_2O_3 or Y_2O_3 with Milli-Q water (5 mL) and trifluoroacetic acid (5 mL). The solution was heated to 80°C until it turned transparent and residual solvents were subsequently evaporated at 120°C. The resulting dry powders, $Nd(CF_3COO)_3$ and $Y(CF_3COO)_3$, respectively, were stored and used to synthesize Ln-doped nanocrystals.

Synthesis of core and core-shell Nanocrystals: The lanthanide-doped nanocrystals were synthesized via a thermal decomposition reaction of trifluoroacetate precursors as described in literature[25]. Briefly, x% 1.25 mmol $Nd(CF_3COO)_3$ and (1-x)% 1.25 mmol $Y(CF_3COO)_3$ were mixed with 1.25 mmol of $Na(CF_3COO)_3$ in a 3-necked 100 mL round flask and dispersed in 1-octadecene (10 mL) and coordinating ligand oleic acid (10 mL). Different relative $Nd(CF_3COO)_3$ concentrations were tested: 1%, 2%, 5% and 10%. The solution was heated to 100◦C while stirring, and then put under a vacuum to remove water and oxygen and purged with N_2. The temperature was increased to 300°C and kept under vigorous stirring for 1 hour. After synthesis, the mixture was cooled to room temperature, precipitated by a mixture of 4:1 acetone and hexane, and collected by centrifugation at 3,000 rpm for 10 min. The precipitate was then washed twice in ethanol. The final precipitate was dispersed in toluene (3 mL), yielding similar NP concentration for every dopant concentration, of around (42 ± 3) mg/mL. For core-shell NP preparation, shell precursors (1 mmol $Y(CF_3COO)_3$ and 1 mmol $Na(CF_3COO)_3$) were dissolved in octadecene (5 mL) and oleic acid (5 mL) to achieve a 0.8:1 shell/core ratio. After core formation, the reaction temperature was lowered to 250◦C and the shell precursor solution was added dropwise to the flask. The temperature was then raised to 305°C and allowed to react until the solution turned transparent (approximately 45 min). The mixture was cooled down to room temperature and the prepared $NaYF_4$:Nd@ $NaYF_4$ (hereafter referred to as Nd-NC@shell) were washed and precipitated according to the previously described protocol, yielding a stable NP solution in toluene of (65 ± 5) mg/mL[26]. Detailed information about the synthesized NPs can be found in Table S1.

Silica-coated Nanocrystals: The Nd-NC@shell nanoparticles were then coated with a silica layer (SiO_2) based on a water-in-oil microemulsion synthesis protocol described elsewhere, with slight modifications[27]. Briefly, IGEPAL® CA-630 (1.3 ml) was dispersed in cyclohexane (10 ml) followed by ultrasonication (20 min). 1 mL of diluted Nd-NC@shell solution in cyclohexane (320 uL NCs + 670 uL cyclohexane) (~ 20 mg/mL) was added to the mixture and stirred for 30 min to homogenize. Then, an aqueous solution of ammonia (30%, 150 µL) was added dropwise, and the solution was stirred for 5 min until it turned completely clear. Lastly, tetraethyl orthosilicate (320 µL of TEOS in cyclohexane 1:4 ratio) was added dropwise. The mixture was stirred for 5 minutes and then left undisturbed overnight to encourage hydrolysis and condensation of the silica precursor. The resulting Nd-NCs@shell@SiO_2 were isolated via centrifugation, washed with ethanol several times, and dispersed in 1 mL of Milli-Q water.

NP structure/composition/charge characterization: As-synthesized colloidal dispersions were diluted in a 1:200 ratio and 6 µL of solution was cast onto TEM grids (300 mesh copper grid) and dried at room temperature. TEM images were collected on an FEI TecnaiF20 microscope (200 kV) (Ian Holmes Imaging Center, Bio21) equipped with energy dispersive X-ray (EDX) detector for sample characterization, including size and chemical composition analysis. NP size was estimated from 100 NPs. Crystal structure analysis was performed by comparing diffraction peaks of the synthesized NPs with X-Ray Diffraction patterns (XRD) of standard host lattices. The plots were obtained by determining the Bragg angle (θ) and plotting the intensity of the diffraction peaks against 2θ. To do so, the Bragg's Law was used to determine the value of θ, where n equals 1, λ is the wavelength of the X-ray and d is the distance between the lattice plane (Equation 1)[28].

$$n\lambda = 2d \cdot sin\theta \qquad (1)$$

NP charge was characterized by zeta potential measurements (Zetasizer, Malvern). The morphology of NPs was further characterized using SEM (HITACHI HD-2000).

Optical Characterization/ Emission Spectra Collection: NIR photoluminescence measurements were performed using a homebuilt system. An 808 nm diode laser (SDL-808-LM-100T, Shanghai Dream Lasers Technology Co., Ltd) and a 785

nm diode laser (SDL-785-LM-100T, Shanghai Dream Lasers Technology Co., Ltd) were used to excite Ln-doped nanocrystals via an inverted optical microscope (Olympus IX-71) in epifluorescence configuration using a half-silvered mirror. The excitation power was around 0.15 mW. The NP luminescence was collected by a 20x objective, separated from excitation light with longpass filters, then guided into a spectrograph/silicon CCD couple (Acton 2150/Princeton 1024B). The luminescence was recorded in the range 725-1000 nm. For generating standard curves for luminescence peak ratio vs temperature, 15 µL of sample (30 mg/mL) was drop-cast onto a round coverslip and placed inside a temperature-controlled stage (Linkam THMS600). Emission spectra were recorded over a temperature range from 25°C to 150°C, at 5°C intervals (at least 2 minutes of temperature equilibration time was applied prior to each measurement). Within the therapeutically relevant range (35-60°C), data was collected at 1°C temperature steps. Acquisition time varied between samples. For sample comparison, raw (integrated) intensity (I) values were corrected for the fraction of excitation light absorbed (F_{abs}), giving a corrected intensity I', based on Equation 2:

$$I' = \frac{I}{F_{abs}} = \frac{I}{(1-10^{-Abs})} \quad (2)$$

Spectra were analyzed using Origin 2023b, and intensity data displayed as means ± standard deviations with error bars indicating one standard deviation.

Cell Culture: A549 cells were cultured in 25 cm^2 culture flasks at 37° C under 5% CO_2 atmosphere. Cells were maintained in DMEM medium with 10% FBS, 1% L-glutamax and 0.1% gentamicin. For fluorescence microscopy experiments, the cells were seeded in 31-mm, glass-bottom dishes (Cellvis, Mountain View, CA, USA) and grown until ~60% confluency before adding the NPs.

Cytotoxicity Studies: NP toxicity was assessed using the cell counting kit-8 (cck-8) assay kit. A549 cells were seeded in a 96-well plate at a density of 5×10^4 cells/well. The next day, 200 µL of increasing concentrations of Nd-NPs@mSi (1, 5, 10, 15, 25 and 50µg/mL) were added to the cells. Three biological replicates were prepared for each condition. Cells incubated with nanoparticles were washed with PBS after 6 h of nanoparticle incubation to remove the non-internalized NPs. After washing, fresh DMEM was added and the sample was incubated for 24 additional hours. After incubation, the cells were washed with medium and 100 µL CCK-8 solution was added to each well and incubated for 1 hour. Absorption values were measured with a microplate reader and normalized to the OD450−OD620 value for the untreated cells.

Single NP emission: Single NP luminescence studies, in films or *in vitro*, were performed using a microspectroscopy apparatus consisting of 785 nm and 808 nm diode lasers coupled to an inverted microscope in epi-fluorescence configuration. The excitation light was focused at the back focal plane of the objective to give wide-field excitation. Emission was collected through the same objective, separated from excitation light by longpass filters, and imaged on a silicon EMCCD camera. Emission from specific diffraction-limited spots was isolated by a slit and spectrally resolved. For film studies, Nd-NC@shell@SiO_2 NPs were diluted in 0.01% (w/v) PEG in MilliQ to a final concentration of 0.6 mg/mL. The solution was then sonicated for 5 min and drop-cast on a glass coverslip. $NaYF_4$:5%Nd@ $NaYF_4$ NPs were diluted in 0.01% (w/v) PMMA in toluene to a final concentration of 0.6 mg/mL The solution was then sonicated for 5 min and spin coated on a glass coverslip. For *in vitro* studies, A549 lung cancer cells were incubated with Nd-NC@shell@SiO_2 (25 µg/mL). Cells were stained with Alexa Fluor 488 Phalloidin. In short, cells were seeded in 31-mm glass-bottom dishes and grown overnight. Next, the cells were fixed with paraformaldehyde (4%) and the membrane was permeabilized with Triton X-100 (0.1%), for 15 min. The sample was carefully washed with PBS (1×) between each step. After washing, 200 µL of phalloidin 488 in 3% BSA solution (1:500 dilution) was added to the dish and the sample was incubated at RT for 30 min. After incubation, the samples were washed twice with PBS (1×).

Statistical Analysis: The data are displayed as means ± standard deviations and error bars indicate standard deviation. A randomization test was used to compare any two groups of values and performed using T-TEST function in Microsoft Excel. Statistical significance was reported as * $p < 0.05$, ** $p < 0.01$, and *** $p < 0.001$.

3. Results and discussion

3.1. Structural Characterization of Nd-NC Nanoparticles

$NaYF_4$:Nd, (Nd-NC) core NPs were synthesized via thermal decomposition of lanthanide precursors[25]. Different Nd^{3+} ion dopant percentages (1%, 2%, 5% and 10%) with respect to the Y^{3+} ion concentration, were tested in order to investigate the impact of increasing Nd^{3+} matrix concentration on the luminescence properties of the resulting NPs. The prepared cores

were then shelled with an inert $NaYF_4$ shell, as core-shell structures have been reported to display improved PL due to the reduced quenching caused by resonance energy transfer between Nd^{3+} optical transitions and C-H and O-H vibrational modes of the solvent[29,30]. All the samples were stable for several months in toluene.

Transmission electron microscopy (TEM) was used to determine NP size and morphology (Fig. 2a-e). Core NPs displayed homogeneous size distribution around 30 nm and polyhedral shape for all the different Nd^{3+} concentrations. NP diameter was independent of the Nd^{3+} concentration, with no visible size changes between the different concentrations (Fig. 2f). The same was observed for the negative control without Nd^{3+} ions (pure NaYF matrix). This is explained by the close match between the ionic radius of Nd^{3+} (r_{Nd}^{3+}=1.123 Å) and Y^{3+} (r_{Y}^{3+}=1.040 Å), preventing significant changes in the crystal structure by doping[31,32]. The addition of the $NaYF_4$ shell led to a significant (~25%) size increase of ~ 9 nm (shell thickness = 4.5 nm) (Fig. 2f), and the resulting Nd-NC@shell NPs displayed uniform size and a more angular morphology compared to Nd-NC cores (Fig. 2e). Elemental analysis was performed to assess the presence of Nd^{3+} and estimate its proportion via Energy Dispersive Spectroscopy (EDS) analysis (Fig. 2g). The obtained atomic percentages showed a strong (linear) correlation between the increasing amount of Nd^{3+} employed in the synthesis, and the final percentage of lanthanide ion in the host matrix (Table S2), indicating successful doping.

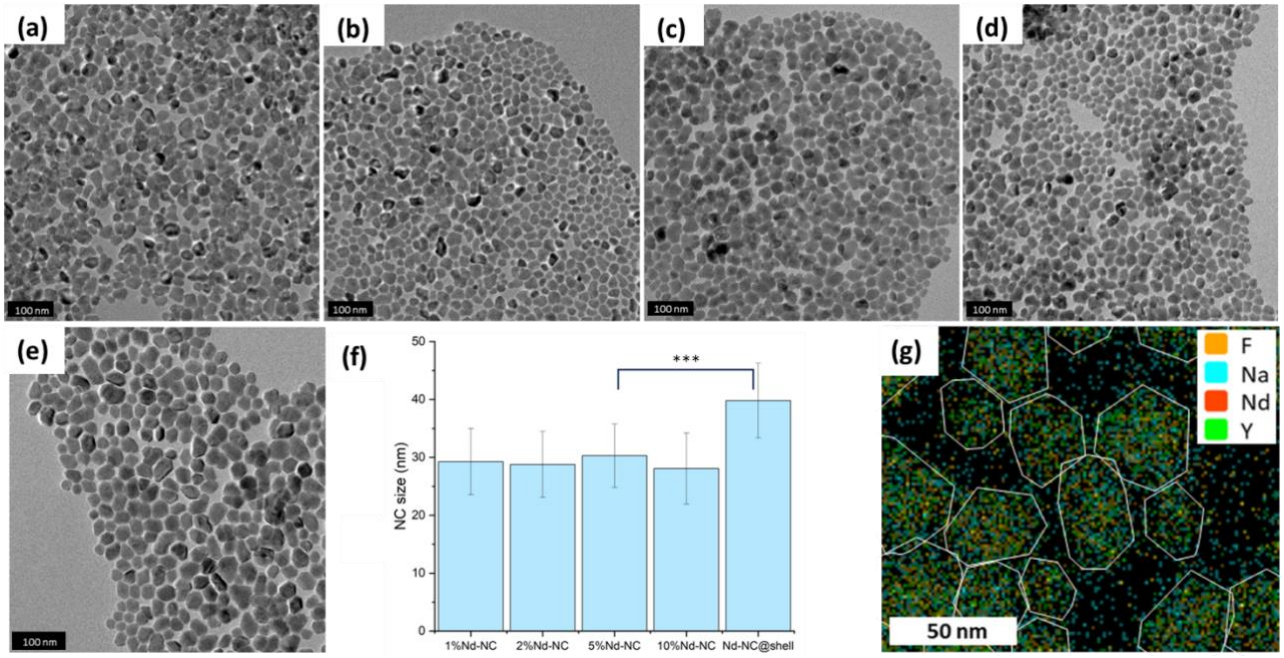

Figure 2| TEM images of Nd-NCs: (a) 1%Nd-NCs; (b) 2%Nd-NCs; (c) 5%Nd-NCs; (d) 10%Nd-NCs; (e) 5%Nd-NCs@shell; (f) size distribution of Nd-NCs with different dopant concentrations and Nd-NC@shell - No significant changes is size were observed for different dopant concentrations (($p > 0.05$), but the size significantly increased with the addition of a $NaYF_4$ shell ($p < 0.05$). NP size was estimated from 100 NPs. Error bars indicate ± SD ; (g) EDS map of Nd-NCs showing the distribution of Nd^{3+} atoms inside the NPs. NP edges were added based on SEM images of the sample;

High-resolution TEM images of individual Nd-NCs (Fig. 3a) revealed clearly distinguishable lattice fringes (3.5 Å (0.35 nm) spacing), indicating a highly crystalline structure in accordance with literature data on $NaYF_4$[33,34]. This structure was further analyzed using selected area electron diffraction (SAED, Fig. 3b), and the results were compared to standard $NaYF_4$ host lattices, which can present two different thermodynamically stable phases, cubic (isotropic) α-phase and hexagonal (anisotropic) β-phase[35]. To do so, d-spacing values for the different NCs were converted to Bragg angle (θ) (Eq. 1). The intensity of the diffraction peaks was plotted against 2θ, enabling a comparison with X-Ray diffraction (XRD) patterns of the standard cubic (COD-1517676) and hexagonal (COD-1517672). host lattices (Fig. 3c). The resulting plot shows a high overlap between the standard peak pattern of the α-cubic phase of $NaYF_4$ and all the as-synthesized NCs (negative control, 1%, 2%, 5%, 10%). Furthermore, the diffraction pattern plots of the synthesized NCs plots show narrow, intense peaks with no anomalous peaks, reflecting a well-defined crystalline structure with no impurities[28,35]. A small shift was observed however for all the peaks compared to the standard $NaYF_4$ phases, which could be attributed to lattice strain in the NPs compared to the bulk material[36]. D-spacing values were obtained for the different diffraction rings of the designed Nd-NCs, and were again in excellent agreement with the standards (Fig. 2d). All of this corroborating data confirms that the synthesized NCs $NaYF_4$ matrix is in the α-cubic phase, and virtually unaffected by Nd^{3+} doping up to 10%.

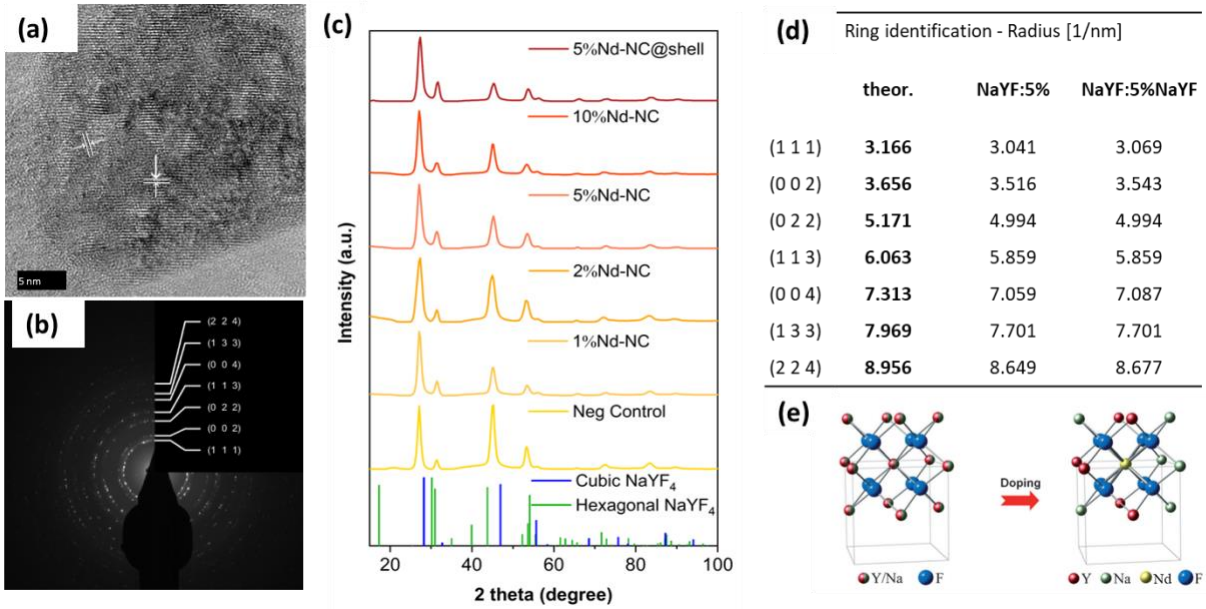

	theor.	NaYF:5%	NaYF:5%NaYF
(1 1 1)	**3.166**	3.041	3.069
(0 0 2)	**3.656**	3.516	3.543
(0 2 2)	**5.171**	4.994	4.994
(1 1 3)	**6.063**	5.859	5.859
(0 0 4)	**7.313**	7.059	7.087
(1 3 3)	**7.969**	7.701	7.701
(2 2 4)	**8.956**	8.649	8.677

Figure 3| (a) High-resolution TEM image of a single 5%Nd-NC showing lattice fringes; (b) SAED of 5%Nd-NC showing the diffraction pattern for different planes (Miller indices noted) – SAED data was analyzed with crystbox[37] ; (c) Diffraction pattern plot of the synthesized Nd-NPs (1%, 2%, 5% and 10%), Nd-NC@shell, as well as the standard cubic and hexagonal $NaYF_4$ standard host lattices, showing a close correlation between the diffraction peaks of synthesized NCs and the standard α-cubic host lattice (in blue); (d) Ring identification for various crystal planes (Miller index noted) of standard cubic $NaYF_4$, $NaYF_4$:5%Nd and shelled $NaYF_4$:5%Nd@$NaYF_4$, showing very close agreement, (e) Graphical representation of the structure of cubic $NaYF_4$ and Nd-NCs (Adapted from [38]).

3.2. Luminescence Properties

Luminescence nanothermometry in cellular environments benefits from brightly luminescent NPs that allow for effective emission readout from lower NP concentrations, reducing the likelihood of concentration-induced toxicity[39]. To optimize PL, the impact of the Nd^{3+} concentration on the emission of the Nd-NCs was studied. Emission spectra were collected for colloidal dispersions at room temperature (RT). Additionally, Nd-NCs were excited at two distinct excitation wavelengths within the first biological window (NIR-I BW), at 785 nm and 808 nm, to evaluate the impact of excitation wavelength on emission. Laser power was kept the same for both wavelengths (0.15 mW). Where possible, for ease of comparison, the same detector acquisition time was used. Alternatively, intensity was standardized using calibration curves determined for Intensity vs. Acquisition Time (Fig S1a, b).

Fig. 4a shows a typical emission spectrum of an Nd-NC sample excited with a 785 nm laser. In this project, we focused on the emission range between 850-920 nm, which includes the reported temperature-dependent emission peaks from the Nd^{3+} in the NIR-I BW[23]. Within this range, four different downshifted peaks can be distinguished, as a result of transitions from different Stark sublevels of the $^4F_{3/2}$ excited state to the $^4I_{9/2}$ ground state, upon NIR excitation of Nd^{3+} (Fig 4b)[16]. It is theorized that Nd^{3+} ions initially undergo the electronic transitions $^4I_{9/2} \rightarrow {}^4F_{5/2}$ and $^4I_{9/2} \rightarrow {}^2H_{9/2}$ upon NIR excitation. Non-radiative relaxation then brings the system to the metastable $^4F_{3/2}$ state before emission occurs[40]. The PL spectra, and integrated emission between 850 and 920 nm, for all the Nd-NCs, the Nd-NC@shell, and the negative control ($NaYF_4$ only) with 785 nm excitation are compiled in Figures 4c and 4e, respectively. For core NPs, an increase in Nd^{3+} concentration resulted in a PL increase of up to the 5%Nd-NCs. However, for 10%Nd-NCs, the PL decreased significantly (by 52%), consistent with literature reports[29,41]. In theory, an increasing dopant concentration should increase PL intensity due to an increase in emitting centers. However, it has been shown that beyond a certain concentration threshold, the shorter distance between Nd^{3+} ions in the $NaYF_4$ lattice promotes non-radiative cross-relaxation described by ($^4F_{3/2}$; $^4I_{9/2}$) → ($^4I_{15/2}$; $^4I_{15/2}$), which decreases overall PL[29,40,42]. A similar trend was observed upon 808 nm laser excitation (Fig 4d, f). 5%Nd-NC displayed the highest emission intensity followed by a 53% intensity loss for 10%Nd-NC. The negative control revealed no luminescence, verifying that the Nd^{3+} dopant is the only emitter in this spectral range. Based on these results, we chose 5%Nd-NC as the best candidate for nanothermometry, as its per-particle emission is highest, allowing for the best emission readouts with the lowest applied NP concentrations.

The impact of an inert (undoped) $NaYF_4$ layer on 5%Nd-NC PL was also evaluated. In agreement with published results, 5%Nd-NC@shell PL increased by 19% for 785 nm excitation and by 10% for 808 nm excitation. As already mentioned, this is a result of a reduction of surface defects near the active core, as well as the increased separation between core Nd ions and the vibrational modes of the solvent. The latter is especially prominent in aqueous environments as the OH stretching mode of water is a powerful quencher of Ln^{3+} excited states[29,30].

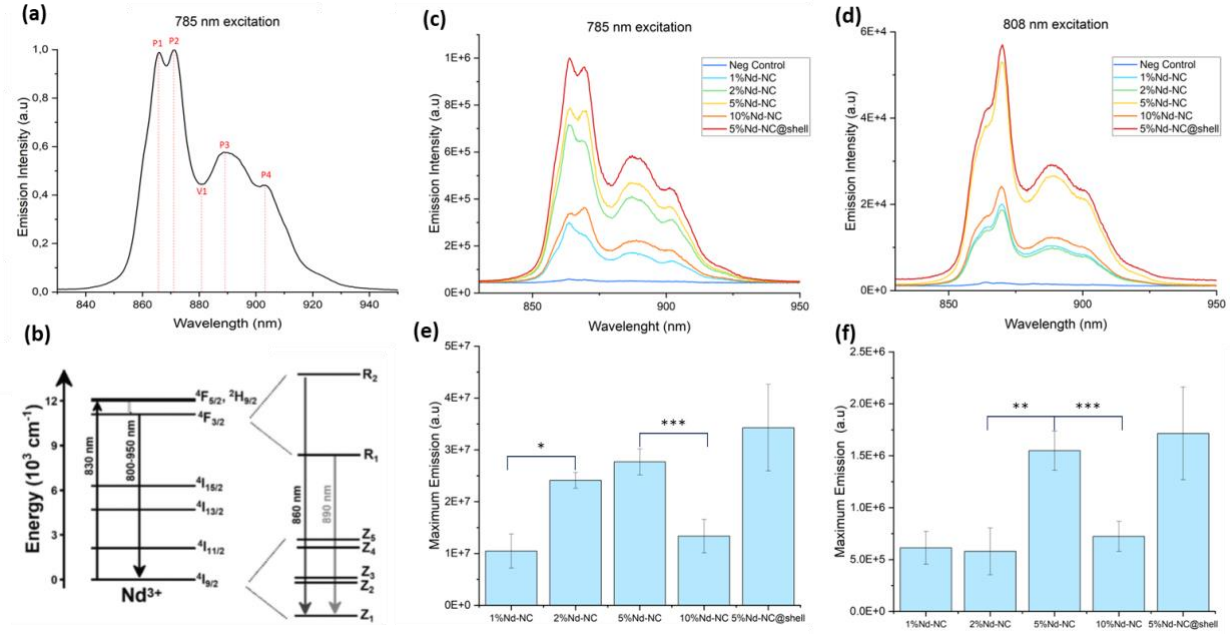

Figure 4| (a) Typical PL spectra of Nd-NCs (upon 785 nm excitation, peak (p) and valley (v) wavelengths referred to in the text are indexed; (b) Schematic energy level diagram showing the Stark-sublevels of $^4F_{3/2}$; $^4I_9/2$ involved in optical absorption and emission of Nd^{3+} after NIR excitation (Adapted from 16); Emission spectra collected for all the NCs upon (c) 785 nm and (d) 808 nm excitation, respectively. Each spectrum is an average of 3 distinct samples (N=3); Bar graphs comparing the integrated area below the emission spectra for each sample upon (e) 785 nm and (f) 808 nm excitation. All the analyzed samples displayed similar concentrations ((42 ± 3) mg/mL, in toluene), therefore for both excitation wavelengths, 5%Nd exhibits the brightest per-particle PL ($p < 0.05$). The addition of an optically inert shell further improved emission intensity by 10-20%. Error bars indicate ± SD

We further compared the corrected PL intensity (I') of the Nd-NCs by adjusting the emission data for the number of photons absorbed for each wavelength (see Eq. 2 in methods). Absorbance spectra for all the samples showed overlapping peaks characteristic of the Nd^{3+} ion, correlated with the $^4I_{9/2} \rightarrow {}^4I_{7/2}$, $^4I_{9/2} \rightarrow {}^4I_{5/2}$ and $^4I_{9/2} \rightarrow {}^4I_{3/2}$ transitions[16]. The spectra revealed a concentration-dependent increase in absorption, with 10%Nd-NC showing the highest absorption at both 785 and 808 nm. Interestingly, the addition of an inert shell led to a slight decrease in optical absorption. I' values were then plotted for core and core-shell NPs, and for both wavelengths (Fig 5b). I' plots for 785 nm excitation reveal concentration-induced self-quenching for dopant concentrations above 2%Nd, with I' decreasing by 52% and 65% when Nd^{3+} concentration is increased from 2%Nd to 5%Nd and from 5%Nd to 10%Nd, respectively. A similar trend is observed for I' upon 808 nm excitation, with I' values decreasing consistently as Nd% increases. While these results pose significant relevance in terms of NP characterization, the absolute emission values were considered more relevant given the biological application of the developed Nd-NCs. The corrected intensity values were also calculated for core-shell structures. In both cases, the shelled NPs displayed a significantly higher I', with a 43% and 54% increase upon 785 nm and 808 nm excitation, respectively. These observations corroborate the conclusions drawn from the absolute emission values and are consistent with the previously mentioned literature reports on the effect of an inert shell on PL[29,30].

From Fig. 5b, Fig. 4c and 4d, it was possible to observe some important differences in emission response upon the two different excitation wavelengths. After 785 nm excitation, Nd-NCs displayed a significantly higher fluorescence compared to 808 nm excitation ($p < 0.05$, for every sample). This can be correlated to the absorbance at these two different wavelengths (Fig. 5a), as all the core and core-shell NPs show higher absorption at 785 nm than 808 nm. Additionally, lower wavelengths are associated with higher energy of the wave. This could also explain the change in spectral shape in the two scenarios. When excited at 785 nm, the intensity of the first and second peak are similar. From Fig 4b, the first peak requires higher energy transitions, and it is therefore facilitated by 785 nm excitation. When excited with 808 nm laser, the intensity of the first peak is significantly lower than the first one, as it requires smaller energetic transitions.

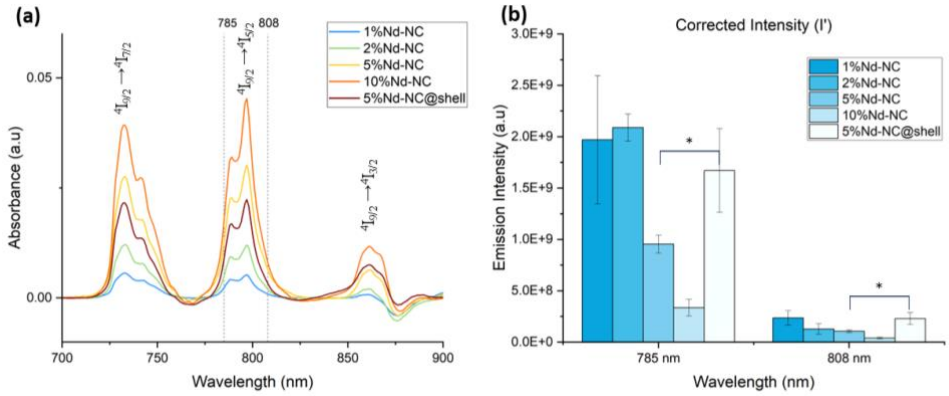

Figure 5| (a) Absorbance spectra of Nd-NCs (1%, 2%, 5%, 10%) and Nd-NC@shell NPs. Absorbance increases with the dopant concentration, and decreases with the addition of a shell (5%Nd-NC vs 5%Nd-NC@shell). All the samples show higher absorbance at 785 nm compared to 808 nm ($p < 0.05$); (b) Corrected emission spectra (I') upon 785 and 808 nm excitation. For 785 nm excitation, I' decreases for concentrations higher than 2%Nd. For 808 nm excitation, I' decreases for dopant concentrations higher than 1%Nd. Independent of excitation wavelength, I' significantly increases for core-shell structures when compared to the active cores ($p < 0.05$). Error bars indicate ± SD

3.1. Temperature Dependence Studies

To analyze the thermosensitive properties of the nanothermometers, PL emission spectra of Nd-NC@shell was collected at different temperatures and the ratios between different peaks were calculated. Luminescent intensity ratios (LIR) of thermally coupled electronic states in Nd-doped NCs are commonly explored in literature for thermal sensing applications. LIR is independent of nanothermometer concentration, excitation intensity and photobleaching, making it a reliable sensing strategy[16,23]. Temperature-dependent NIR emission spectra at 785 nm and 808 nm excitation are presented in Fig. 6a and 6b, respectively. Data was normalized ([0,1]) to the emission maximum in this region. Temperature-dependent studies were also performed for 5%Nd-NC core NPs (Fig S2 a-d), and similar results were obtained.

Nd-NC@shell showed clear temperature-dependent emission, as indicated by the color gradient in Fig. 6a and b. These plots indicate four peaks (P1-P4) and one valley (V1) as candidates for LIR temperature calibration. For each excitation wavelength, we investigated four combinations of these peaks and valleys (P1/P2, P1/P3, P1/P4 and P1/V1), listing their fit parameters in Table S3. At 785 nm excitation, LIR P1/V1 provided the most accurate calibration, with the highest coefficient of determination of 0.93 using a linear fit (Fig. 6c). At 808 nm excitation, P2/P1 yielded the best calibration curve (r^2=0.97) (Fig. 6d). In addition, a high linear correlation (r^2=0.94) within the biologically relevant thermal range (25 - 60°C) was observed for 808 nm, indicating a higher accuracy for NP-HT applications. We attribute this higher correlation to improved accuracy as a consequence of larger spectral shifts which results in a relative signal to noise improvement. The observed results show that Nd-NC@shell particles display high sensitivity to temperature changes in the BW-I, and this observation is in agreement with previously reported studies using Nd-doped $NaYF_4$ NCs, which show a similar spectral shape between 850 and 920 nm and a temperature dependent LIR trend characteristic of Nd^{3+} in a $NaYF_4$ matrix[40]. Hence the as-synthesized NCs demonstrate clear potential to be used as nanothermometers for NP-HT applications.

Figure 6| Temperature dependence plots obtained for Nd-NC@shell NPs upon (a) 785 nm and (b) 808 nm laser excitation. Emission spectra for all the samples were collected at increasing temperatures, starting at 25°C with a 5°C increase until 150°C. For the biologically relevant temperature range (35-60°C), spectra were collected at 1°C intervals. Data is shown as an average of 3 acquired spectra (N=3). Calibration curves were derived by calculating LIR vs temperature for 785 nm (c) and 808 nm (d) excitation. A higher linear correlation was obtained for samples excited at 808 nm excitation (r^2=0.97)

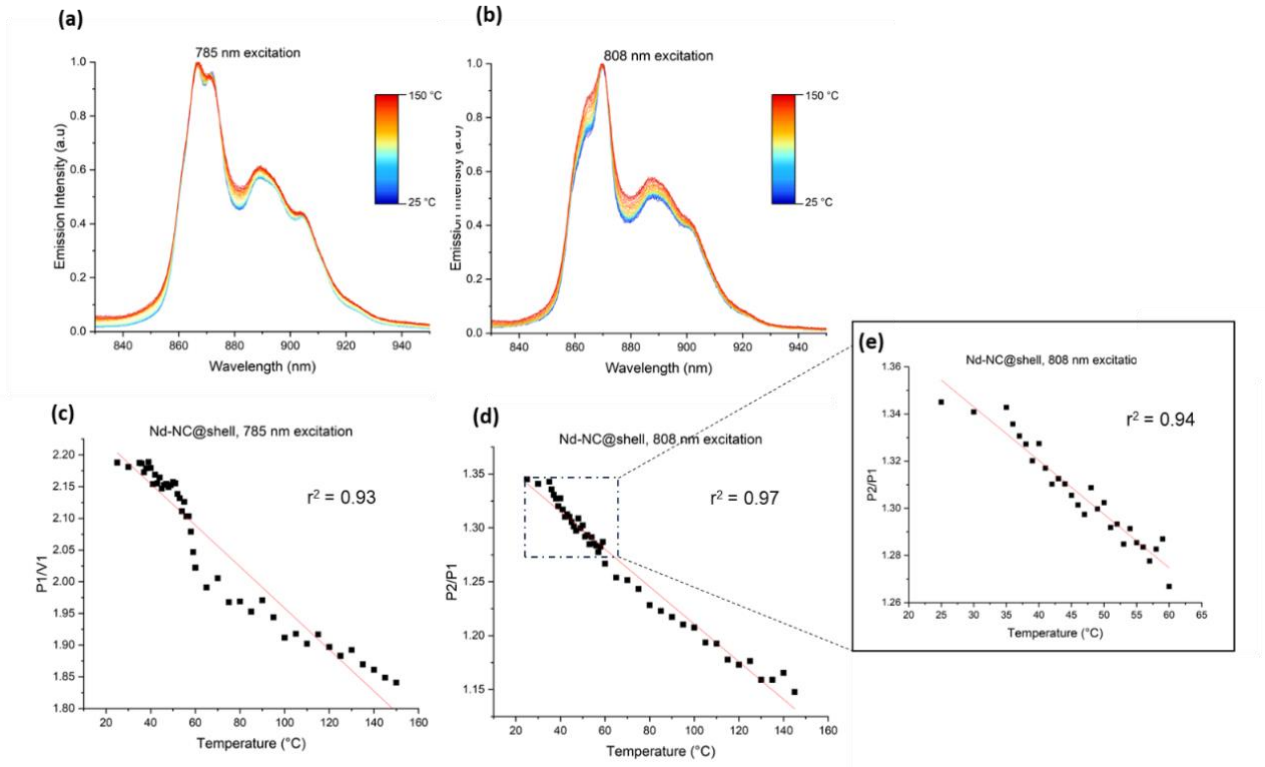

compared to 795 nm excitation (r^2=0.93). A zoomed in calibration curve focused on a HT-relevant temperature range (20-60°C) upon 808 nm excitation also revealed high correlation (r^2=0.94). Curves shown on graph c was obtained by plotting P1/V1, while graphs d and e were plotted from P2/P1.

3.2. Biocompatibility

The Nd-NCs were synthesised in an organic phase, and exhibit a surface coated with oleic acid (OA), which reduces stability in aqueous solutions and biocompatibility. For biological applications, it is essential to modify the NP surface to mitigate these effects. The addition of a silica layer is a common approach used in biological studies because silica is biocompatible, has excellent chemical stability and is low cost. In addition, it facilitates the subsequent functionalization with different functional groups for improved uptake[43,44]. In this work, a silica shell (SiO_2) was added to $NaYF_4$:5%Nd@$NaYF_4$ NCs using the reverse microemulsion technique. In this process, IGEPAL® CA-630 is used as an amphiphilic surfactant for micelle formation in an organic solvent, with hydrophobic groups on the outside and hydrophilic groups inside the micelle. The addition of OA-stabilized NP leads to a ligand exchange between OA and IGEPAL® CA-630, and the micelle is subsequently expanded upon ammonia addition to the solution. Lastly, TEOS is added to the solution and hydrolyzed, replacing IGEPAL® CA-630 and chemically absorbing on the NP surface. After condensation of the hydrolyzed TEOS, the SiO_2 shell is formed, and the NPs can be washed and redispersed in an aqueous solution[43].

3.2.1. Characterization of SiO_2-coated Nd-NCs

The success of the SiO_2-coating protocol was assessed via TEM and SEM (Fig 13a). Nd-NC@shell@SiO_2 showed homogeneous shape and an average size of (68 ± 8) nm. It was also possible to observe the encapsulation of single crystals inside the silica shell, with a shell thickness of ~15 nm. Lastly, TEM and SEM images revealed the absence of free SiO_2 NPs, indicating that the ratio between TEOS and Ln-NCs was adequate to coat the NC surfaces. Nd-NC@shell@SiO_2 displayed a negative surface potential of (-46.1 ± 1.2) mV, consistent with the existence of partially deprotonated hydroxyl groups on the SiO_2 surface[44].

To investigate the influence of SiO_2 on emission, PL spectra of the uncoated Nd-NC@shell and coated Nd-NC@shell@SiO_2 were compared at 785 and 808 nm excitation (0.1 mW excitation power). Fig 7. c and e show the normalized spectra ([0,1]) of Nd-NC@shell before and after SiO_2 coating, showing no significant changes to the spectral shape. Hence, the previously obtained calibration curves for Nd-NC@shell can be used for thermal analysis using Nd-NC@shell@mSi NPs. Non-normalized PL spectra measured for a similar NP concentration (~ 60 mg/mL) suggest that the addition of a SiO_2 leads to a PL increase for both laser excitation wavelengths. Similar to what was observed for the addition of an inert $NaYF_4$ shell to the active Nd^{3+}- doped core, we hypothesize that the deposition of an additional protective layer

leads to a passivation effect that further shields the core from solvent-induced quenching[29,30]. However, the shelled and unshelled NC quantum yields should be determined to better evaluate the effect of the SiO_2 layer on overall PL.

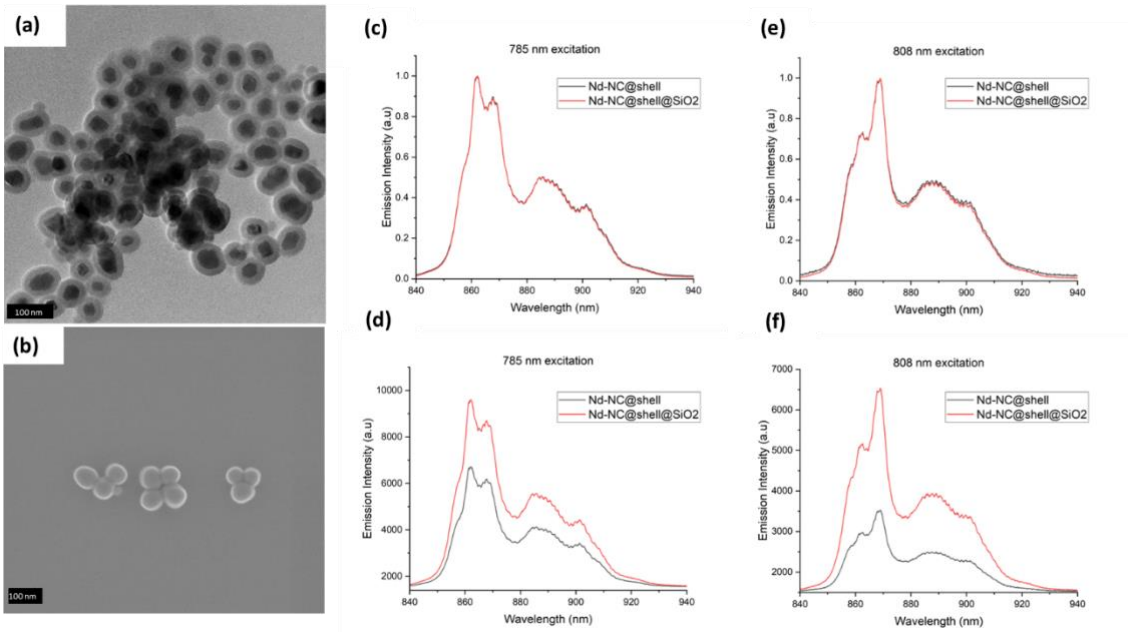

Figure 7| (a) TEM and (b) SEM image of $NaYF_4$:5%Nd@$NaYF_4$@SiO_2; Normalized PL spectra of bare and SiO_2-coated NPs at (c) 785 and (d) 808 nm excitation; Black lines correspond to the normalized emission spectra of bare Nd-NC@shell, while Nd-NC@shell@SiO_2 emission spectra are shown in red.

3.2.2. Cytotoxicity Assays

To prove that the presence of the nanothermometers inside the cells does not affect cell viability, Nd-NC@shell@SiO_2 toxicity was evaluated using a well-established WST-8 assay. Different concentrations of Nd-NC@shell@SiO_2 (ranging between 1 and 50 µg/mL) were incubated with A549 lung cancer for 6 h. Figure 8 shows the calculated viability normalized for the negative control. For the tested concentrations, there was no significant decline in cell proliferation after incubation with NPs, and cell survival rate was higher than 85% for all the tested concentrations. These results are consistent with other reported studies using SiO_2-coated $NaYF_4$ NCs for similar NP concentrations[45,46]. These *in vitro* results confirm that the SiO_2 layer endows the nanothermometers with relatively low cytotoxicity, allowing for safe thermal monitoring in biological environments.

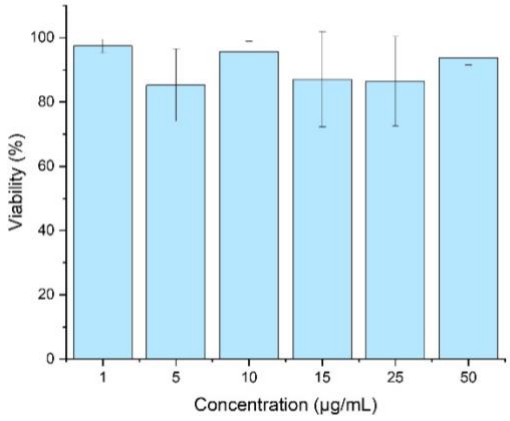

Figure 8| Viability of A549 cells after 6-h incubation with different concentrations of Nd-NC@shell@SiO_2. Cells that were not incubated with NPs were used as a control, representing 100% viability. Error bars indicate ± SD.

3.3. Single Nanoparticle Optical Thermometry

One of the current bottlenecks of Ln-NC applications is the lack of literature data reporting the emission behavior on a single particle level. Most studies are based on the analysis of bulk samples, neglecting discrepancies in optical properties

of individual NPs[47]. Furthermore, single NP spectra enables the assessment of thermal sensitivity of luminescent NPs in a biologically relevant manner. Upon cellular uptake, NPs are dispersed inside the cytoplasm at low concentrations. This could potentially limit nanothermometric potential due to insufficient emission signal. To further validate the potential of the designed Nd-NCs, we performed single NP optical thermometry in NCs internalized by cancer cells. A549 cells were incubated with Nd-NC@shell@SiO_2 (25 µg/mL) for 3 hours, and the cells were then stained with Alexa Fluor 488 Phalloidin. Spectral mapping was performed for two distinct channels – NP and cell detection channels. NPs were excited using a 808 nm laser excitation and the cell-staining dye was excited at 488 nm (Fig. 9c and d). From these images, it was possible to see the overlap between the two channels, showing that the NCs were indeed located in the cells. Spectral maps were compared with widefield This images were compared with a widefield image of the sample (Fig. 9a). The overlap between Nd-NC@shell@SiO_2 mapping and widefield+cell mapping images, we could observe that the NPs were located in the cell. Results also revealed a significant amount of internalization by the A549 cancer cells, crucial for the viability

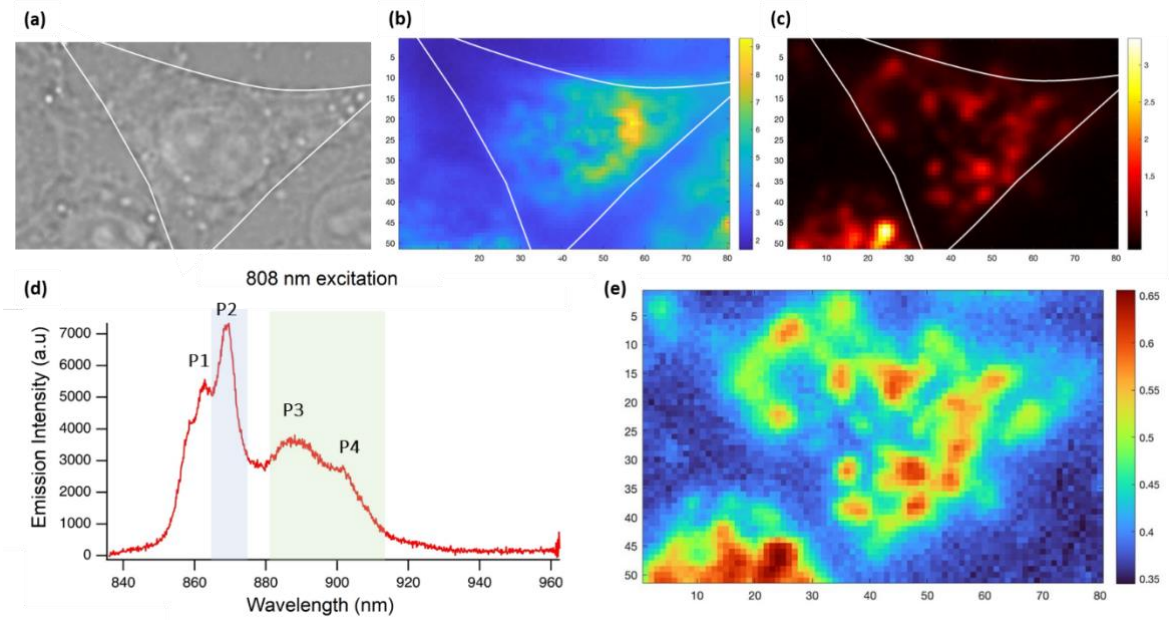

of these particles as temperature probes in NP-HT.

Figure 9| (a) Widefield microscopy image of A549 cells after incubation with Nd-NC@shell@SiO_2 NPs. Spectral mapping was obtained for (b) cell-dye staining (Ex: 488 nm) and for (c) NPs (Ex: 808 nm.showing overlap between the two channels. (d) Spectra was collected for single NPs, and 4 distinct peaks (P1-P4) could be detected. Spectral analysis was performed by integrating the area below the graph for P2 and P3+P4, shown in blue and green, respectively. (e) Color-coded map of the ratiometric analysis of P2/(P3+P4).

Using optical spectroscopy, the emission spectra of a single NP was then collected at different temperatures within a biological relevant range (Fig 9c). From these results, it was possible to observe a change in spectral shape with the temperature increase.

4. Conclusion and Future Prospects

In this study, we present the synthesis and characterization of biocompatible core-shell $NaYF_4$ nanocrystals doped with Nd^{3+} for deep tissue nanothermometry applications, with excitation and emission wavelengths located within the first biological transparency window. Nanocrystals were prepared via thermal decomposition, resulting in a crystalline structure and homogeneous size distribution. Photoluminescence was optimized by tuning the active dopant concentration, showing that PL increases with Nd^{3+} concentration up to a certain threshold (5%). Emission was further enhanced by the addition of an inert $NaYF_4$ shell. Temperature-dependence was studied by determining the luminescent intensity ratios (LIR) at different temperatures. High linear correlation was obtained, displaying the excellent thermal sensitivity of Ns-NCs at 785 and 808 nm excitation. To render the Nd-NCs biocompatible, the as-synthesized core-shell structures were coated with a silica layer, resulting in cell viabilities > 85% when incubated with up to 50 µg/ml Nd-NC@shell@SiO_2 over 6 hours. Finally, luminescent thermal readout was demonstrated *in vitro* in A549 cells by spectrally resolving the diffraction-limited luminescence spots from single particles over a clinically relevant temperature range from 20-50 °C. The demonstration of

biocompatible, nano-localized, NIR thermometry in cells is a significant step in the development of viable hyperthermal cancer treatments.

5. Acknowledgements

The authors are thankful to the Global PhD partnership program between KU Leuven and Melbourne university (GPUM/21/025). MB, SZ, PM, and JAH thank the Australian Government for funding through the Australian Research Council (ARC) Centre of Excellence in Exciton Science (CE170100026). JAH acknowledges an ARC Future Fellowship award (FT180100295). BF, HU and SR acknowledged the financial support from Research Foundation of Flanders (FWO) research grants (G0D4519N, G081916N, VS08523N), postodoctoral fellowship (for BF, 12X1419N and 12X1423N), and from the KU Leuven (C14/15/053, C14/19/079, C14/22/085). We acknowledge the Ian Holmes Imaging Centre, Bio21 Institute, University of Melbourne for electron microscopy undertaken in this work.

6. References

1. Fernandes, S. *et al.* Magnetic Nanoparticle-Based Hyperthermia Mediates Drug Delivery and Impairs the Tumorigenic Capacity of Quiescent Colorectal Cancer Stem Cells. *ACS Appl. Mater. Interfaces* **13**, 15959–15972 (2021).
2. Khafaji, M., Zamani, M., Golizadeh, M. & Bavi, O. Inorganic nanomaterials for chemo/photothermal therapy: a promising horizon on effective cancer treatment. *Biophys Rev* **11**, 335–352 (2019).
3. Adhipandito, C. F., Cheung, S.-H., Lin, Y.-H. & Wu, S.-H. Atypical Renal Clearance of Nanoparticles Larger Than the Kidney Filtration Threshold. *IJMS* **22**, 11182 (2021).
4. Sun, T. *et al.* Engineered Nanoparticles for Drug Delivery in Cancer Therapy. *Angew. Chem. Int. Ed.* n/a-n/a (2014) doi:10.1002/anie.201403036.
5. Karakotchian, M. & Fraser, I. S. An ultrastructural study of microvascular inter-endothelial tight junctions in normal endometrium. *Micron* **38**, 632–636 (2007).
6. Ruman, U., Fakurazi, S., Masarudin, M. J. & Hussein, M. Z. Nanocarrier-Based Therapeutics and Theranostics Drug Delivery Systems for Next Generation of Liver Cancer Nanodrug Modalities. *IJN* **Volume 15**, 1437–1456 (2020).
7. Bahrami, B. *et al.* Nanoparticles and targeted drug delivery in cancer therapy. *Immunology Letters* **190**, 64–83 (2017).
8. Chatterjee, D. K., Diagaradjane, P. & Krishnan, S. Nanoparticle-mediated hyperthermia in cancer therapy. *Therapeutic Delivery* **2**, 1001–1014 (2011).
9. Hannon, G., Tansi, F. L., Hilger, I. & Prina-Mello, A. The Effects of Localized Heat on the Hallmarks of Cancer. *Adv. Therap.* **4**, 2000267 (2021).
10. Elming, P. *et al.* Hyperthermia: The Optimal Treatment to Overcome Radiation Resistant Hypoxia. *Cancers* **11**, 60 (2019).
11. Phung, D. C. *et al.* Combined hyperthermia and chemotherapy as a synergistic anticancer treatment. *J. Pharm. Investig.* **49**, 519–526 (2019).

12. Beik, J. *et al.* Nanotechnology in hyperthermia cancer therapy: From fundamental principles to advanced applications. *Journal of Controlled Release* **235**, 205–221 (2016).

13. Kok, H. P. *et al.* Heating technology for malignant tumors: a review. *International Journal of Hyperthermia* **37**, 711–741 (2020).

14. Tosi, D., Poeggel, S., Iordachita, I. & Schena, E. Fiber Optic Sensors for Biomedical Applications. in *Opto-Mechanical Fiber Optic Sensors* 301–333 (Elsevier, 2018). doi:10.1016/B978-0-12-803131-5.00011-8.

15. Beccaria, A. *et al.* Temperature monitoring of tumor hyperthermal treatments with optical fibers: comparison of distributed and quasi-distributed techniques. *Optical Fiber Technology* **60**, 102340 (2020).

16. Nexha, A., Carvajal, J. J., Pujol, M. C., Díaz, F. & Aguiló, M. Lanthanide doped luminescence nanothermometers in the biological windows: strategies and applications. *Nanoscale* **13**, 7913–7987 (2021).

17. West, C. L., Doughty, A. C. V., Liu, K. & Chen, W. R. Monitoring tissue temperature during photothermal therapy for cancer. *Journal of Bio-X Research* **2**, 159–168 (2019).

18. Ring, E. F. J. & Ammer, K. Infrared thermal imaging in medicine. *Physiol. Meas.* **33**, R33–R46 (2012).

19. del Rosal, B., Ximendes, E., Rocha, U. & Jaque, D. In Vivo Luminescence Nanothermometry: from Materials to Applications. *Advanced Optical Materials* **5**, 1600508 (2017).

20. Zhou, J., del Rosal, B., Jaque, D., Uchiyama, S. & Jin, D. Advances and challenges for fluorescence nanothermometry. *Nat Methods* **17**, 967–980 (2020).

21. Quintanilla, M. & Liz-Marzán, L. M. Guiding Rules for Selecting a Nanothermometer. *Nano Today* **19**, 126–145 (2018).

22. Schäfer, H., Ptacek, P., Kömpe, K. & Haase, M. Lanthanide-Doped $NaYF_4$ Nanocrystals in Aqueous Solution Displaying Strong Up-Conversion Emission. *Chem. Mater.* **19**, 1396–1400 (2007).

23. Bednarkiewicz, A., Wawrzynczyk, D., Nyk, M. & Strek, W. Synthesis and spectral properties of colloidal Nd3+ doped NaYF4 nanocrystals. *Optical Materials* **33**, 1481–1486 (2011).

24. Tsang, M. Y. *et al.* Pr^{3+} doped $NaYF_4$ and $LiYF_4$ nanocrystals combining visible-to-UVC upconversion and NIR-to-NIR-II downconversion luminescence emissions for biomedical applications. *Nanoscale* **14**, 14770–14778 (2022).

25. Boyer, J.-C., Vetrone, F., Cuccia, L. A. & Capobianco, J. A. Synthesis of Colloidal Upconverting $NaYF_4$ Nanocrystals Doped with Er^{3+}, Yb^{3+} and Tm^{3+}, Yb^{3+} via Thermal Decomposition of Lanthanide Trifluoroacetate

Precursors. *J. Am. Chem. Soc.* **128**, 7444–7445 (2006).

26. Prorok, K. *et al.* The impact of shell host ($NaYF_4$ /CaF_2) and shell deposition methods on the up-conversion enhancement in Tb^{3+} , Yb^{3+} codoped colloidal α-$NaYF_4$ core–shell nanoparticles. *Nanoscale* **6**, 1855–1864 (2014).
27. Silva, M. O., Kirkwood, N., Mulvaney, P., Ellis, A. V. & Stok, K. S. Evaluation of a lanthanide nanoparticle-based contrast agent for microcomputed tomography of porous channels in subchondral bone. *Journal Orthopaedic Research* **41**, 447–458 (2023).
28. Chen, G., Ohulchanskyy, T. Y., Kumar, R., Ågren, H. & Prasad, P. N. Ultrasmall Monodisperse $NaYF_4$:Yb^{3+} /Tm^{3+} Nanocrystals with Enhanced Near-Infrared to Near-Infrared Upconversion Photoluminescence. *ACS Nano* **4**, 3163–3168 (2010).
29. Skripka, A. *et al.* Inert Shell Effect on the Quantum Yield of Neodymium-Doped Near-Infrared Nanoparticles: The Necessary Shield in an Aqueous Dispersion. *Nano Lett.* **20**, 7648–7654 (2020).
30. Kar, A. & Patra, A. Impacts of core–shell structures on properties of lanthanide-based nanocrystals: crystal phase, lattice strain, downconversion, upconversion and energy transfer. *Nanoscale* **4**, 3608 (2012).
31. Darshan, G. P. *et al.* Neodymium doped yttrium aluminate synthesis and optical properties – A blue light emitting nanophosphor and its use in advanced forensic analysis. *Dyes and Pigments* **134**, 227–233 (2016).
32. Ramakul, P., Supajaroon, T., Prapasawat, T., Pancharoen, U. & Lothongkum, A. W. Synergistic separation of yttrium ions in lanthanide series from rare earths mixture via hollow fiber supported liquid membrane. *Journal of Industrial and Engineering Chemistry* **15**, 224–228 (2009).
33. Wang, L. *et al.* A New Cubic Phase for a $NaYF_4$ Host Matrix Offering High Upconversion Luminescence Efficiency. *Advanced Materials* **27**, 5528–5533 (2015).
34. Wang, F. *et al.* Selective Heteroepitaxial Nanocrystal Growth of Rare Earth Fluorides on Sodium Chloride: Synthesis and Density Functional Calculations. *Angew Chem Int Ed* **51**, 8796–8799 (2012).
35. Klier, D. T. & Kumke, M. U. Analysing the effect of the crystal structure on upconversion luminescence in Yb^{3+} ,Er^{3+} -co-doped $NaYF_4$ nanomaterials. *J. Mater. Chem. C* **3**, 11228–11238 (2015).
36. Dolabella, S., Borzì, A., Dommann, A. & Neels, A. Lattice Strain and Defects Analysis in Nanostructured Semiconductor Materials and Devices by High-Resolution X-Ray Diffraction:

Theoretical and Practical Aspects. *Small Methods* **6**, 2100932 (2022).

37. Klinger, M. & Jäger, A. *Crystallographic Tool Box* (*CrysTBox*): automated tools for transmission electron microscopists and crystallographers. *J Appl Crystallogr* **48**, 2012–2018 (2015).
38. Tu, D. *et al.* Breakdown of Crystallographic Site Symmetry in Lanthanide-Doped $NaYF_4$ Crystals. *Angewandte Chemie* **125**, 1166–1171 (2013).
39. Sukhanova, A. *et al.* Dependence of Nanoparticle Toxicity on Their Physical and Chemical Properties. *Nanoscale Res Lett* **13**, 44 (2018).
40. Maciejewska, K. & Marciniak, L. The role of Nd3+ concentration in the modulation of the thermometric performance of Stokes/anti-Stokes luminescence thermometer in NaYF4:Nd3+. *Sci Rep* **13**, 472 (2023).
41. Laia, A. S. *et al.* Nd3+ doped Y2O3 micro- and nanoparticles: A comparative study on temperature sensing and optical heating performance within the 1st biological window. *Optical Materials* **142**, 114126 (2023).
42. Renero-Lecuna, C. *et al.* Nd^{3+} -Doped Lanthanum Oxychloride Nanocrystals as Nanothermometers. *J. Phys. Chem. C* **125**, 19887–19896 (2021).
43. Ureña-Horno, E., Kyriazi, M.-E. & Kanaras, A. G. A method for the growth of uniform silica shells on different size and morphology upconversion nanoparticles. *Nanoscale Adv.* **3**, 3522–3529 (2021).
44. Van Zundert, I. *et al.* Versatile and Robust Method for Antibody Conjugation to Nanoparticles with High Targeting Efficiency. *Pharmaceutics* **13**, 2153 (2021).
45. Abdul Jalil, R. & Zhang, Y. Biocompatibility of silica coated NaYF4 upconversion fluorescent nanocrystals. *Biomaterials* **29**, 4122–4128 (2008).
46. Xu, S. *et al.* Mesoporous silica coating NaYF4:Yb,Er@NaYF4 upconversion nanoparticles loaded with ruthenium(II) complex nanoparticles: Fluorometric sensing and cellular imaging of temperature by upconversion and of oxygen by downconversion. *Microchim Acta* **185**, 454 (2018).
47. Dong, H., Sun, L.-D. & Yan, C.-H. Upconversion emission studies of single particles. *Nano Today* **35**, 100956 (2020).

a